IEEE Robotics and Automation Letters (RA-L) paper, presented at ICRA 2026, Vienna, Austria. Cite as RA-L paper.

Modular Actuator for Multimodal Proprioceptive and Kinesthetic Feedback of Robotic Hands

Sungwoo Park, Myo-Taeg Lim, and Donghyun Hwang, *Member, IEEE*

***Abstract*— This study addresses the challenge of implementing proprioceptive and kinesthetic (PK) feedback in robotic hands, essential for grasping and manipulation tasks in unstructured environments. We developed a compact modular actuator featuring a low-module, high-transmission-ratio multistage gear mechanism that measures 25×10×24 mm, weighs only 10 grams, and maintains moderate backdrivability. The actuator provides multimodal PK feedback, capturing position, velocity, current, and torque data, which are critical for performing various grasping and manipulation tasks. To enable precise motion and force control, we introduced a new adaptive velocity estimator and a simplified Reaction Torque Observer (RTOB). Comprehensive experiments demonstrated the actuator's ability to accurately detect surface shape, roughness, and stiffness of target objects, eliminating the need for additional sensors or space. Experimental results confirmed the actuator's precision, achieving measurement errors of 5.8 mrad for position, 0.19 rad/s for velocity, and 0.011 N·m for torque. These findings highlight the actuator's ability to leverage proprioceptive information, significantly enhancing the functionality and adaptability of robotic hands in diverse and dynamic scenarios.**

I. Introduction

Robotic grasping and manipulation tasks are typically executed in a well-structured environment with pre-defined objects [1], [2]. This is because the external characteristics of an object, such as its size, position, pose, and shape, can be easily obtained using a robotic vision system. However, obtaining an object's intrinsic characteristics, such as stiffness, weight, and fragility, which are usually recognized through physical interactions with the environment/object, is difficult using visual information alone. These intrinsic characteristics aid in grasping unknown objects. In humans, somatosensory feedback, including tactile, proprioceptive, and kinesthetic feedback, is used to obtain non-visual feedback [3], [4]. Among this feedback, proprioceptive and kinesthetic feedback (PK feedback) takes priority over tactile information. This is because PK feedback encompasses crucial feedback about both movement and interaction forces, essential for executing tasks that involve physical contact, such as grasping and manipulation.

This paper was recommended for publication by Editor Ashis Banerjee upon evaluation of the Associate Editor and Reviewer's comments.

This work was supported in part by Korea Advanced Research Program through the Samsung Science and Technology Foundation (SRFC-IT2202-01), in part by the Industrial Strategic Technology Development Program (RS-2024-00442029) funded by the Ministry of Trade, Industry and Energy (MOTIE, Korea), and in part by the KIST Institutional Program. (Corresponding author: Donghyun Hwang.)

Sungwoo Park and Donghyun Hwang are with the Center for Humanoid Research, KIST, Seoul 02792, South Korea, Sungwoo Park and Myo-Taeg Lim are with the Department of Electrical and Computer Engineering, Korea University, Seoul 02841, South Korea (e-mail: donghyun@kist.re.kr)

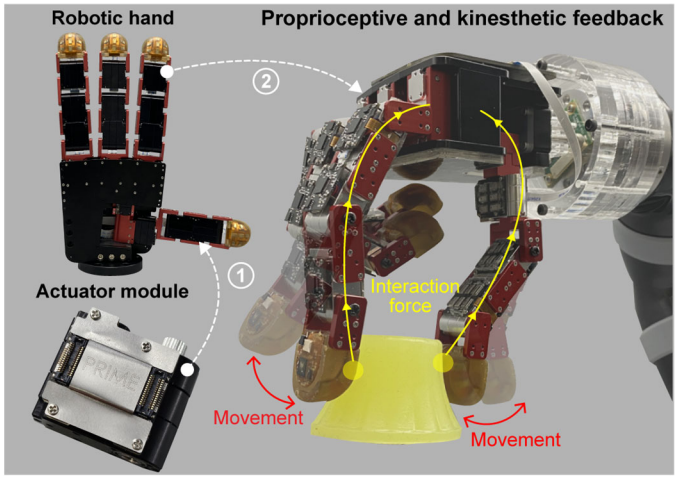

Fig. 1. The robotic hand capable of proprioceptive and kinesthetic feedback with the embedded actuator modules.

In humans, PK feedback is obtained from sensory receptors, which are known as proprioceptors located in joints, tendons, and muscles [4]. These receptors mainly sense movement, position of body parts, and muscle tension [5]. This information is translated into the joint position, velocity, and interaction force/torque (F/T) at the joints of robotic systems. Recent studies have been conducted to implement PK feedback in robots based on this knowledge [6]–[11].

Developing actuator systems for robotic hands that can provide PK feedback presents significant challenges, particularly in comparison to larger robotic applications [6]–[11]. These challenges stem primarily from the limited space and weight capacities available at the ends of robotic manipulators where robotic hands are typically mounted. Such constraints limit the incorporation of various components such as actuators, mechanisms, and sensors. Furthermore, these actuators must exhibit high torque density and sensing accuracy to reliably perform grasping and manipulation tasks. Considering these requirements, Table I summarizes actuators that have been used in robotic hand applications, including both commercial and research-based designs. The comparison focuses on key specifications such as size, weight, torque, sensing capabilities, and level of integration, which are critical factors for end-effector performance in compact and high-DOF robotic hands [12]–[19].

A five-finger robotic hand with a parallel mechanism was introduced in [12]. It enhances backdrivability and high-payload capabilities. However, embedding position sensors in each joint is challenging and may limit PK feedback precision. The lack of actuator-level modularity could also complicate maintenance. A series elastic gripper proposed in [13] handles unstructured disturbances and estimates

TABLE I
A COMPARISON BETWEEN PREVIOUS ACTUATOR FOR ROBOTIC APPLICATIONS AND OUR PROPOSED MODULAR ACTUATOR

Ref.	Actuator (Core)	Transmission Mechanism (ratio)	Dimension [mm]	Weight [g]	Max. Torque [N·m]	No load speed [RPM]	Power density [W/kg]	Actuator feedback information	Modularity*
[12]	DC (Coreless)	PG[3] (16:1)	8 × 8 × 30	12	0.0098	806	69.1	PI[5]	X (DAQ[9], MD[10])
[13]	DC (-)	MG[1] (-)	42 ×34 × 62	85	2	-	-	PI[5]	X (DAQ[9])
[14]	BLDC (-)	HD[2], TP[4] (210:1)	41 × 21 × 13	30	0.672	28	65.7	PI[5], CI[6]	X (DAQ[9], MD[10])
[15]	DC (-)	MG[1] (369:1)	36 × 20 × 25	40	0.71	90	167.3	PI[5], CI[6]	X (DAQ[9], MD[10])
[16]	DC (Iron)	MG[1] (254:1)	32 × 50 × 40	55	1.5	59	168.5	PI[5]	O
[17]	BLDC (-)	MG[1] (218:1)	34 × 16 × 49	45	1.31	100	304.9	PI[5]	O
[18]	DC (Iron)	MG[1] (238:1)	36 × 24 × 27	17	0.39	114	274	PI[5]	O
[19]	DC (Coreless)	MG[1] (288:1)	34 × 20 × 26	23	0.93	81	343	PI[5], CI[6], VI[7]	O
Ours	DC (Coreless)	MG[1] (644:1)	25 × 10 × 24	10	0.32	109	365.3	PI[5], CI[6], VI[7], TI[8]	O

1: Multistage gear mechanism; 2: Harmonic drive mechanism; 3: Planetary gear mechanism; 4: Timing belt and pulley mechanism;
5: Position information; 6: Current information; 7: Velocity information; 8: Torque information; 9: Data acquisition device; 10: Motor driver;
*: Embedding the sensor, driver, communication, and data acquisition device within the actuator (see Fig. 2 and 3).

interaction forces effectively. However, the elastic components limit its performance and may require recalibration for objects of different sizes and shapes. The joint direct-drive robotic hand in [14] uses harmonic drives, pulley mechanisms, magnetic position sensors, and a F/T sensor for finger impedance control. The complex transmission system and limited modularity may restrict it to two actuators per finger despite its features. Bulkiness also poses a challenge. A fully actuated, joint direct-drive, four-finger robotic hand with 16 degrees of freedom (DOF) was introduced in [15]. It focuses on mechanical simplicity with small actuators. However, its performance may be affected by complex wiring, low power density, and reduced positioning accuracy due to traditional potentiometers.

Commercially available compact actuators also exist [16]–[19]. These actuators are modularly designed. They integrate gear mechanisms, motors, and electronics into a single unit. This design simplifies wiring and maintenance and is suitable for high-DOF robotic hands. However, actuators in [16]–[18] are limited to position sensing due to the lack of torque sensors. As a result, providing PK feedback, which requires both torque and velocity information, is challenging. Their internal position controllers further restrict precise force-controlled grasping and manipulation. The actuator in [19] is compact and lightweight. It offers position, current, and velocity feedback. However, its ability to provide accurate reaction torque and velocity information remains unverified.

We propose an actuator module capable of multimodal sensing, providing position, velocity, current, and torque information for precise PK feedback. Designed to be compact and lightweight, the module is well-suited for robotic hand applications. To achieve this, we adopted a multistage gear mechanism and a coreless motor, offering moderate backdrivability and high-power density. All electrical systems are integrated within the actuator to simplify the design and enhance maintenance and connectivity. Additionally, we implemented an adaptive velocity estimator and a simplified Reaction Torque Observer (RTOB) to enable precise calculation of velocity and torque information. Using this advanced actuator module, we developed a 16-DOF fully actuated robotic hand with four fingers, capable of delivering multimodal PK feedback, as shown in Fig. 1.

The main contributions of this study are as follows:.

1) Design and validation of a compact, lightweight actuator module with integrated sensing and control, optimized for use in space-constrained robotic hands.
2) Development of an adaptive velocity estimator and a simplified reaction torque observer (RTOB) for real-time estimation of position, velocity, current, and torque without external sensors.
3) Experimental verification of the actuator's capabilities through stiffness measurement and surface shape and roughness detection using integrated feedback.

II. Design of the Modular Actuator

A. Configuration of Mechanical Components

In robotic hand applications, actuators are expected to satisfy several key criteria. First, high power density is important, as robotic hands serve as end-effectors and significantly influence the overall payload performance of the system. Second, a compact design is necessary to accommodate multiple degrees of freedom within limited space, enabling dexterous manipulation similar to that of a human hand. Third, backdrivability is crucial for effective force control during interactions with objects. This is particularly vital because integrating multiple sensors in a confined space is challenging and costly, making backdrivability a practical approach for achieving force control.

To develop a compact and lightweight actuator with high power density, we employed a multistage gear mechanism with a higher gear ratio than traditional designs. Typical ratios range from 200 to 400 over 3 to 5 stages [15]–[19]. However, increasing the gear ratio presents challenges, such as reduced output speeds below 50 rpm and decreased backdrivability, impacting the actuator's responsiveness to external forces. To address these challenges, we analyzed the factors affecting backdrivability, as shown in Fig. 2(a)–(d). The backdrivability is characterized by the backdriving torque (T_{bck}):

$$T_{bck} = J_{bck}\alpha_{out} + T_{fric} + T_{motor} \quad (1)$$

where J_{bck}, α_{out}, T_{bck}, T_{fric}, and T_{motor} represent the backdriving moment of inertia, acceleration on the actuator's output side, backdriving torque, friction torque, and motor torque, respectively. To minimize the backdriving torque, it is essential to reduce the backdriving inertia. The backdriving inertia is inversely proportional to the square of the speed reduction ratio. Furthermore, the inertial properties of gears and pinions significantly affect backdriving performance. As the pitch circle radius of the gear and pinion increases, the inertia scales with the fourth power of the radius [20].

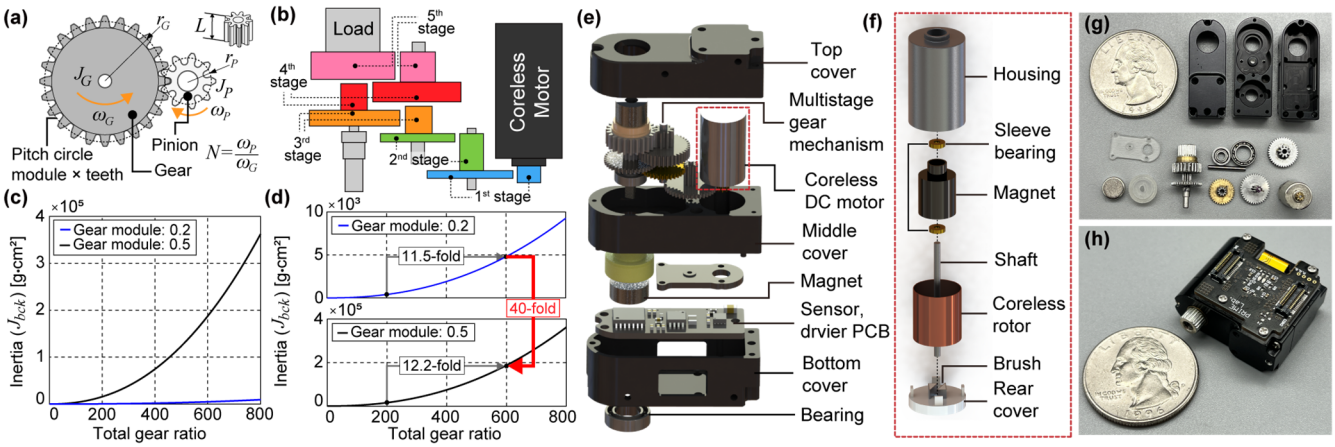

Fig. 2. Design concept of the actuator based on the multistage transmission mechanism. (a) and (b) are schematics of the spur and multistage gear transmission mechanism for the actuator, respectively. (c) and (d) show the backdriving inertia analysis results for gear module and ratio effects. (e) and (f) represent the exploded views of the components of the proposed actuator and the coreless motor inside the actuator module, respectively. (g) and (h) show the overall mechanical components of the actuator and the fully assembled actuator, respectively.

To quantitatively evaluate the factors influencing backdrivability, we used a reflected inertia model to compute the backdriving moment of inertia. This analysis considered how adjustable design parameters, such as gear ratio and gear module, affect the rotational inertia of the gear train. As shown in Fig. 2(c) and (d), the gear module had a more significant impact than the gear ratio. For instance, increasing the gear ratio from 200 to 600 results in a 12-fold increase in the backdriving moment of inertia, while increasing the gear module from 0.2 to 0.5, with the same number of gear teeth, leads to a nearly 40-fold increase. The minimum gear module of 0.2 was selected to ensure manufacturability. These findings highlight the critical importance of minimizing the gear module to maintain backdrivability, even when higher gear ratios are employed. Although applying a higher gear ratio than conventional designs can reduce output speed and potentially affect responsiveness to external forces, this issue was mitigated by employing a coreless DC motor with low inertia and high-speed capabilities. This strategy offsets the negative effects of speed reduction while improving overall performance [21]. By integrating low-inertia gear sets with this motor, the design achieves higher gear ratios while minimizing the deterioration of backdrivability.

Fig. 2(e) and (f) show the components of the proposed actuator and the coreless DC motor, respectively. The coreless DC motor (PL-710PA, HOFON MOTOR) was custom-designed with a no-load speed of approximately 69,000 rpm and a stall torque of over 6.0 g·cm. Commercial gear sets from a servo motor (HV75K, MKS) were used to achieve a speed reduction ratio of approximately 644:1. The gear modules are 0.2 for the first four stages and 0.3 for the fifth stage, with all components made of 7075 aluminum. The overall components of the actuator module are shown in Fig. 2(g). The fully assembled actuator shown in Fig. 2(h) measures 25 × 10 × 24 mm and weighs 10 g. Its compact size and lightweight design are suitable for robotic hands.

B. Configuration of Electrical Components

Compact actuators for robotic hand applications face several challenges, including reduced sensor accuracy, complex wiring, limited communication bandwidth, and the need for externally mounted motor drivers. These limitations, especially in terms of communication latency, can hinder responsiveness during contact-based manipulation tasks. While consolidating all electronics onto a central PCB inside the palm may lead to a more compact design in certain anthropomorphic hand configurations, we chose a distributed, modular architecture to ensure broader applicability and design flexibility. By embedding sensing and control electronics within each actuator, our approach minimizes external wiring, simplifies integration, and supports scalability across a wide range of robotic platforms, including simple grippers and fully actuated multi-DOF hands.

As shown in Fig. 3(a–c), the actuator includes two PCBs: the top board houses bidirectional connectors for serial communication, flat cable connectors, and a microcontroller (STM32F401CC, ST), while the bottom board integrates a DC motor driver (DRV8838, TI), a shunt resistor, a current amplifier (MAX40056, Analog Devices), and an absolute magnetic sensor (AS5047, AMS). The two boards are interconnected via a flexible flat cable, with the top board handling signal processing, communication, and control.

To achieve high-speed communication with external devices, the Serial Peripheral Interface (SPI) protocol was used, as shown in Fig. 3(d). A magnetic absolute position sensor and current amplifier were integrated to ensure high signal bandwidth and precise data acquisition for position and current. For current sensing, a shunt resistor-based method, shown in Fig. 3(e), was employed to accommodate the compact design of the actuator module while maintaining high bandwidth and measurement accuracy. However, the shunt resistor-based method introduces significant fluctuations in the current signal due to the pulse-width modulation technique, which complicates accurate current measurement. To address this, a synchronized current measurement technique was implemented, as illustrated in Fig. 3(f). This method measures the current signal I_{DS} at the midpoint between the turn-on signal of V_{GS} and the turn-off signal of V_{DS}, enabling precise signal capture at frequencies up to 20 kHz.

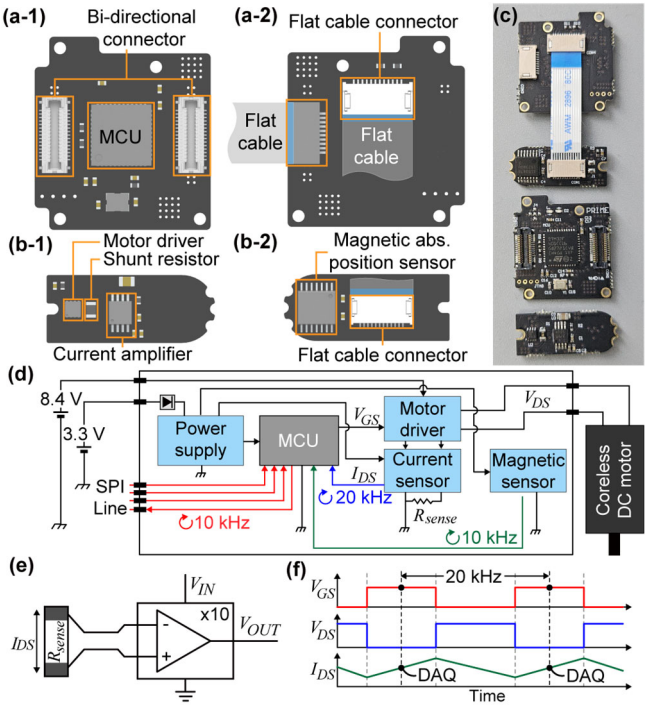

Fig. 3. Overview of the electrical configurations of the proposed actuator module. (a-i) and (b-i) are the top and bottom PCBs of the actuator module, respectively. (c) shows the fabricated PCBs. (d) illustrates the communication and sensing structure of the actuator module. (e) and (f) indicate the shunt-based and PWM synchronized current sensing method, respectively.

III. Proprioceptive and Kinesthetic Feedback Capability

PK feedback refers to multimodal sensory information, including position, velocity, and torque at the joints. Accurately capturing this data typically requires additional sensors, which can increase the actuator's size, weight, and cost—especially in compact designs. To address this, we integrate PK feedback directly into the actuator, enabling precise measurement without extra sensors. An observer-based adaptive velocity estimator ensures accurate velocity estimation, and reaction torque is distinguished using complementary position, velocity, and current data. The effectiveness of this approach is validated through dedicated experiments for each feedback type.

A. Position and Current Feedback

To evaluate the position-sensing performance of the proposed actuator, the experimental setup included a reference encoder (E50S8-8000-6-L-5-C, Autonics) and a coupling, as shown in Fig. 4(a). For the experiment, a permanent magnet with a thickness of 2.5 mm and a diameter of 6 mm (NdFeB-9049, Radial Magnets) was attached to the output shaft of the actuator module. The diameter of the magnet is critical, as a smaller diameter can result in significant off-axis misalignment and positional errors. Additionally, the airgap, defined as the axial distance between the sensor and the magnet, is equally important. A smaller airgap can lead to electrical or magnetic saturation, while a larger airgap can reduce positioning accuracy due to local field deflection. In our experiment, the airgap was set to approximately 0.5 mm based on preliminary experiment.

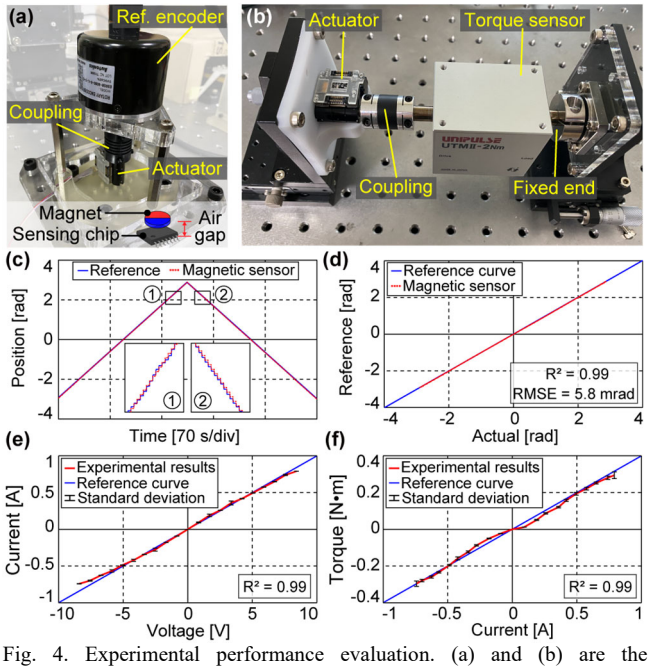

Fig. 4. Experimental performance evaluation. (a) and (b) are the experimental setups for position and torque experiments, respectively. (c) and (d) show the experimental results of a position measurement performance of magnetic position sensor. (e) and (f) indicate the results of current measurement to an applied voltage and measured torque, respectively.

The experimental results, shown in Fig. 4(c) and (d), indicate that both sensors achieved a linearity of approximately 0.99. The root-mean-square error (RMSE) for the magnetic position sensor was measured at 5.8 mrad. These findings demonstrate that the proposed magnetic position sensor delivers high positioning accuracy. Furthermore, the actuator design, utilizing a non-contact position sensor, eliminates frictional torque, ensuring wear-free operation and consistent performance over time.

We conducted a static torque test to validate the relationship between voltage, current, and torque. The experimental setup included a torque sensor (UTM II, UNIPULSE) connected to the actuator via a rubber coupling, as shown in Fig. 4(b). To evaluate the correlation between applied voltage, current, and torque, we performed five repetitions of the test. The results, presented in Fig. 4(e) and (f), show that the current data from the actuator exhibited a linear relationship with both the applied voltage and measured torque, with a linearity of 0.99 for both. Minor discrepancies observed in the data may be attributed to manufacturing variances or nonlinear friction effects. The detailed sensing performance and specifications of the actuator are summarized in Table II.

B. Adaptive Velocity Estimator for Velocity Feedback

In robotic hand applications, compact actuators directly interact with objects or environments, making precise control and rapid responsiveness essential. Commonly used control schemes, such as PID and PD controls, heavily depend on accurate joint velocity estimation [24]. For compact actuators, installing sensors within the actuator for velocity estimation poses significant challenges. Typically, compact actuators rely on encoders or potentiometers mounted on the output shaft to achieve high positional accuracy. However, due to the

TABLE II. SPECIFICATIONS OF DEVELOPED ACTUATOR MODULE

		Specifications	Value	Unit
Actuator module		Size	25 × 10 × 24	mm
		Weight	10	g
		No-load speed	109	RPM
		Stall torque	0.32	N·m
		Input voltage	8.4	V
Sensing performance	Current	Range	± 0.9	A
		Resolution	10	mA
		Max. Sampling Freq.	20	kHz
	Torque	Range	± 0.32	N·m
		RMSE	0.011	N·m
		Max. Sampling Freq.	10	kHz
	Position	Range	± 3.14	Rad
		RMSE	5.8	mrad
		Max. Sampling Freq.	10	kHz
	Velocity	Range	± 11.4	rad/s
		RMSE	0.19	rad/s
		Max. Sampling Freq.	10	kHz

low output speeds caused by high gear ratios, these actuators struggle to obtain precise velocity information. The most widely used method for velocity estimation involves position measurements, expressed as $\omega=(\theta(kT)-\theta((k-1)T))/T$, where, ω is the estimated velocity, $\theta(kT)$, and $\theta((k-1)T)$ are the current and previous sampled positions, and T is the sampling period. Although this method is simple, its accuracy is significantly affected by quantization noise in the position measurements.

To address these challenges, methods such as neural network-based joint velocity estimation [22] and observer-based estimators for servo motor drives [23] have been proposed. The method in [22] uses a neural network as a filter, leveraging current and historical data to reduce control errors in multi-DOF systems. However, its high computational cost, due to two hidden layers with 100 nodes each, makes it impractical for embedded systems in compact actuators. In [23], an observer-based velocity estimator was introduced, using position and current data instead of numerical differentiation. Although more efficient than neural networks, this approach relies heavily on accurate models and manual tuning, which limits robustness.

To overcome these limitations, we propose a robust velocity estimator with a similar observer structure but adaptive parameter adjustment. Unlike conventional observers, our approach uses a recursive least squares (RLS) algorithm to automatically update gain parameters, eliminating the need for precise prior modeling and manual tuning. This enhances robustness and simplifies deployment in real-world applications. The estimator also maintains low computational overhead and real-time performance, making it well-suited for compact embedded systems.

The previously developed observer estimated velocity using position and current measurements. It avoided the numerical differentiation process, which significantly reduced accuracy due to quantization noise. However, it required manual tuning of five parameters: torque constant, inertia, and proportional, integral, and derivative gains. Our proposed velocity estimator simplifies this process. It uses only three gain parameters, as shown in Fig. 5(a), and eliminates the need for modeling parameters and manual tuning. To achieve this, the recursive least squares (RLS) algorithm [24] is integrated

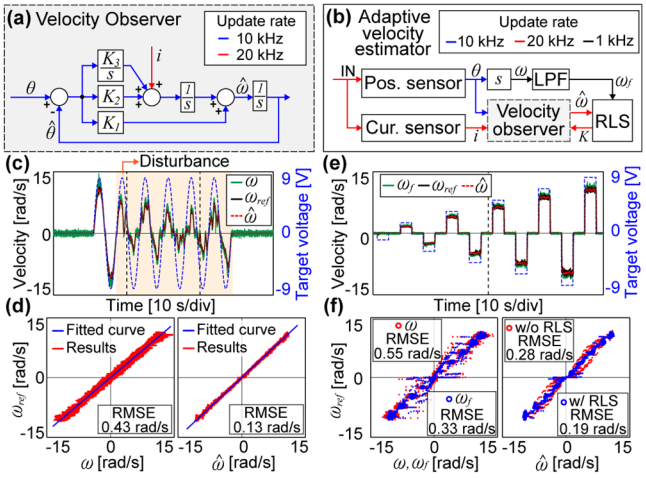

Fig. 5. Block diagram and experimental results of the proposed velocity estimator are shown. (a) depicts the velocity observer estimating velocity using position and current data. (b) outlines the structure of the proposed adaptive velocity estimator. (c) and (d) present experimental results evaluating velocity estimation performance under arbitrary disturbances applied to the actuator. (e) and (f) provide a quantitative comparison of velocity estimation performance among the numerical differentiation method, simple filter, velocity observer, and the proposed adaptive velocity estimator under step input conditions.

into the observer structure. This enables the automatic determination of optimal parameters.

The structure of the proposed adaptive velocity estimator is shown in Fig. 5(b). The system takes inputs from a position sensor and a current sensor. The position signal (θ) is passed through a differentiation block to calculate the velocity (ω), which is then processed by a low-pass filter with a cutoff frequency of 50 Hz. This filtering step reduces noise and enhances signal quality. The filtered velocity (ω_f) and the current measurement (i) are input to the velocity observer, which estimates the velocity ($\hat{\omega}$). The observer is integrated with the RLS algorithm, which dynamically adjusts the gain vector (K) to minimize errors between the filtered velocity (ω_f) and the estimated velocity ($\hat{\omega}$). This adaptive process ensures robust and accurate velocity estimation. The proposed velocity estimator operates in real-time with a maximum update rate of 10 kHz, matching the update rate of the positional information. Despite the use of the RLS algorithm, the estimator maintains low computational complexity and is lightweight enough to run on embedded systems, preserving real-time performance at 10 kHz.

To evaluate the performance of the proposed velocity estimator, experiments were conducted using the setup shown in Fig. 4(a). The reference velocity (ω_{ref}) was measured by a reference encoder, while the other velocity data were calculated by the actuator module. The first experiment assessed the robustness and accuracy of the proposed velocity estimator, as shown in Fig. 5(c). A sinusoidal target voltage was applied to generate actuator velocity, and an arbitrary external disturbance was introduced to the output shaft of the actuator after approximately 8 seconds. This disturbance caused significant fluctuations in the actuator's velocity. Despite the disturbance, the estimated velocity closely matched the reference velocity, whereas the velocity calculated using numerical differentiation showed significant errors due to quantization noise. The experimental results are presented in Fig. 5(d). The RMSE between the calculated

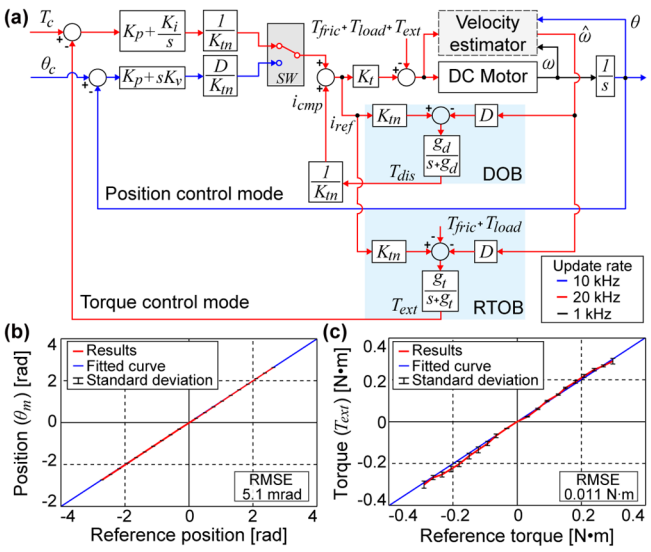

Fig. 6. Block diagram and experimental results of a mode switching controller. (a) illustrates the position and torque mode switching controller based on the simplified DOB, RTOB, and velocity estimator. (b) and (c) are the experimental results on the position and torque controller, respectively.

velocity and the reference velocity was approximately 0.43 rad/s, while the RMSE between the estimated velocity and the reference velocity was significantly lower at approximately 0.13 rad/s. These results demonstrate that the proposed velocity estimator effectively reduces velocity errors, even under external disturbances.

The velocity estimation performance is significantly affected by sudden changes, such as step input responses. To evaluate the robustness of the proposed estimator, we conducted an experiment using an asymptotically increasing step signal as the target voltage, as shown in Fig. 5(e). In this test, both the calculated and filtered velocities were measured, and we compared the performance of the estimator with and without the RLS algorithm.

The results, presented in Fig. 5(f), show that the RMSE of the measured velocity was approximately 0.55 rad/s. Applying a low-pass filter (cutoff frequency of 50 Hz) reduced the RMSE to 0.33 rad/s. Using the estimator without the RLS algorithm, the RMSE was further reduced to 0.28 rad/s. With the RLS algorithm integrated, the RMSE decreased to 0.19 rad/s. These results confirm that the proposed velocity estimator, particularly with the RLS algorithm, significantly improves estimation accuracy under dynamic conditions.

C. *Simplified Reaction Torque Observer for Torque Feedback*

An accurate torque measurement capability is essential for robotic hand applications, as torque control is critical for managing interaction forces during tasks such as gripping, manipulation, and contact-based operations. Precise torque measurement ensures effective force control, contributing to stability, safety, and efficiency. However, achieving accurate torque data in compact actuators is challenging due to limited space, which makes integrating additional torque sensors impractical. To overcome this challenge, we developed a torque estimator that provides torque feedback using position, velocity, and current data. Position and current data are used for the velocity estimator, while estimated velocity data are utilized for the RTOB as shown in Fig. 6(a). All this information is obtained through internal sensors and the estimator integrated into the proposed actuator module.

To further enhance torque measurement, we propose a simplified RTOB method inspired by previously developed simplified disturbance observer (DOB) [25]. Conventional RTOB methods require acceleration data derived from numerically differentiating velocity information [26]. However, accurately measuring acceleration in compact actuators with high transmission ratios is difficult, similar to the challenges faced by the velocity estimator. Our simplified RTOB estimates external interaction torque using only current and velocity data, eliminating the need for acceleration data. The external interaction torque (T_{ext}) is calculated as the difference between the following components: the product of the reference current and nominal torque constant (K_{tn}), the product of the estimated velocity and zero-order constant (D), the estimated friction torque (T_{fric}), and the load torque (T_{load}). Friction and load torque are determined through a simple motion test. By utilizing velocity data from our adaptive velocity estimator, the simplified RTOB method provides external reaction torque measurement in real-time, with the same update rate as the velocity estimator.

To evaluate the performance of the proposed RTOB and actuator systems, we implemented a mode-switching controller, as depicted in Fig. 6(a). This controller allows manual toggling between position and torque modes, which are commonly employed in robotic hand applications. The controller integrates simplified DOB and RTOB to enhance system robustness and operates at control frequencies of 10 kHz for position and 20 kHz for torque, respectively. We conducted experiments to assess the control performance of the actuator, as shown in Fig. 6(b) and (c). The experimental results indicate that the position controller aligns closely with the reference position, achieving an RMSE of 5.1 mrad. Although the torque controller exhibited minor errors, potentially due to inaccuracies in the simplified RTOB, these are within the acceptable range for estimating external torque by using current information. The measured RMSE for the torque controller is approximately 0.011 N·m.

IV. Proprioceptive Feedback for Robotic Fingers

In this study, we developed a compact actuator module capable of measuring multimodal proprioceptive and kinesthetic (PK) feedback, including position, velocity, and torque. This feedback helps detect object characteristics that are difficult to identify visually, enabling more delicate and adaptive interaction. By integrating PK information, the system can better understand properties such as texture and stiffness, which are essential for precise manipulation. To validate its effectiveness, we built a 16-DOF robotic hand using the proposed actuators and conducted experiments on stiffness measurement and surface shape and roughness detection, as shown in Figs. 7 and 8.

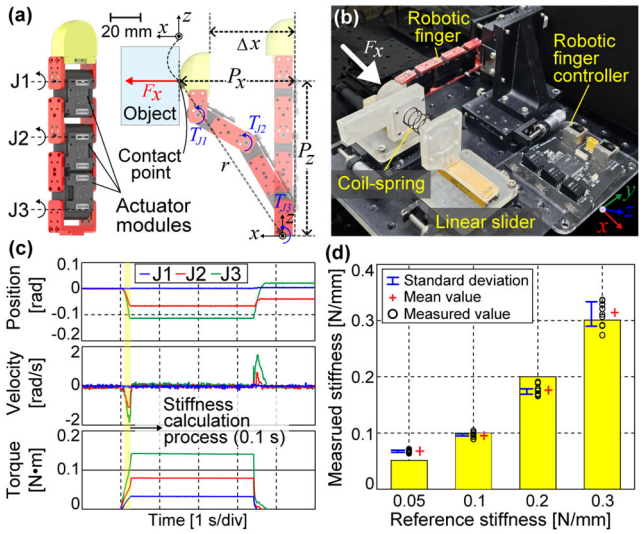

Fig. 7. Experimental setup and results of a stiffness measurement. (a) illustrates the configuration and coordination system of a robotic finger. (b) is the experimental setup. (c) and (d) are the experimental results on stiffness measurement capability.

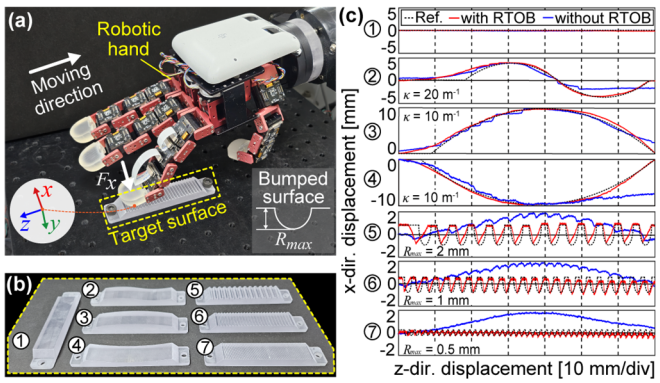

Fig. 8. Experimental setup and results of a surface shape and texture detection. (a) is the experimental setup. (b) displays seven surfaces with varying shapes and roughness levels. (c) illustrates the reconstructed surfaces based on information detected by the robotic finger, comparing the results with and without the reaction torque observer.

A. *Stiffness Measurement Capability*

We evaluated the practical effectiveness of the actuator through a stiffness measurement experiment, using the setup shown in Fig. 7(a) and (b). The experimental system consisted of a robotic finger, a controller, two low-friction linear sliders (LS852, THK), and four coil springs with known stiffness values ranging from 0.05 to 0.3 N/mm. A force was applied in the x-direction (F_x), and the resulting displacement (Δx) was measured, as depicted in Fig. 7(a). Fingertip forces were calculated using the Jacobian matrix, $T = J^T F$, and targeted torques were controlled for each actuator using a previously developed mode-switching controller. The displacement (Δx), finger radius (r), and fingertip positions (P_x and P_z) were then determined using the forward kinematics of the robotic finger.

The results of the position, velocity, and torque measurements for each actuator during the experiment are presented in Fig. 7(c). The controller determined the stiffness of the coil springs in real-time using a linear regression approach, completing the process within 0.1 seconds for 1000 samples. During the experiment, J1 was set to position control mode, while J2 and J3 operated in torque control mode. This configuration was critical for maintaining the fingertip's contact position and generating the linear motion necessary to calculate the linear stiffness of the coil spring. Additionally, the robotic finger was aligned perpendicular to gravity to eliminate the influence of gravitational effects.

Fig. 7(d) presents the results of ten repeated stiffness measurements for each spring, with the RMSE of the measured stiffness calculated as 0.02 N/mm. The variation in measured stiffness increases with larger reference stiffness values. The observed errors are likely caused by inconsistencies at the contact points due to the 3D-shaped fingertip. These errors could potentially be mitigated by integrating tactile sensors at the fingertip to more accurately detect its contact position, thereby enhancing the overall accuracy of stiffness measurements.

B. *Surface Shape and Roughness Detection Capability*

A commonly used method for humans to detect surface shape and roughness involves lateral hand scanning [27], which relies heavily on human PK feedback. This task poses challenges for robots, as it requires precise detection of fine displacements while maintaining contact force and adapting to the surface's shape. We tested the effectiveness of a robotic hand equipped with our developed actuator, specifically assessing the robotic finger's ability to detect surface shape and roughness using PK feedback.

In the experiment, we prepared seven different 3D-printed surfaces, as shown in Fig. 8(b). For surface shape detection, we used a flat surface, a wave surface with a curvature of 20 m^{-1}, and both convex and concave surfaces with a curvature of 10 m^{-1}. For roughness detection, we created three bumped surfaces with peak heights (R_{max}) of 2 mm, 1 mm, and 0.5 mm, respectively. As depicted in Fig. 8(a), the robot arm moved vertically in the z-direction while the robotic finger pressed against each surface in the x-direction. Throughout this interaction, the finger consistently adjusted to the contours of each surface, guided by the contact force control of each actuator. After laterally scanning each specimen, we reconstructed the height profile of each surface, as illustrated in Fig. 8(c). To validate the performance of the previously developed RTOB-based torque controller, we conducted experiments with and without the application of RTOB and compared the resulting height profiles. In the experiment without RTOB, all joints exerted the same target voltage.

The experimental results show that the reconstructed surface shapes closely matched the reference surface shapes when the RTOB was applied. However, minor phase errors observed at the start of each experiment were attributed to the initial acceleration of the robotic arm. Without the RTOB, the reconstructed surface shapes deviated significantly from the ground truth, highlighting the difficulty of exerting a linear force without the torque controller. These findings demonstrate that the robotic hand can distinguish surface curve features as small as 10 m^{-1} and detect roughness as fine as 0.5 mm. Additionally, the proposed PK feedback and controller effectively enable the robotic hand to identify object characteristics. While these results were achieved using only proprioceptive information from the robotic hand, integrating a tactile sensor at the fingertip could further improve the

accuracy and performance of surface shape and roughness detection.

V. Conclusion

This study presented the development of a compact and lightweight actuator module for robotic hand applications. The actuator, featuring a low-module, high-ratio multistage gear transmission, fits within a 25 × 10 × 24 mm form factor and weighs only 10 grams, while providing moderate backdrivability and reliable multimodal proprioceptive and kinesthetic (PK) feedback. To enhance velocity estimation, we proposed an adaptive estimator combining a velocity observer and a recursive least-squares algorithm, which improved accuracy over conventional methods. Based on this, a simplified reaction torque observer and a mode-switching controller were implemented, enabling precise position and torque control. The actuator's performance was validated through experiments on stiffness measurement and surface texture and shape detection using a 16-DOF robotic hand.

For future work, we aim to automate the calibration process for the torque observer and enhance grasping stability through the integration of tactile and PK sensors. We also plan to apply the actuator to various end-effector mechanisms and develop adaptive grasping algorithms that utilize somatosensory feedback for better object interaction.

References

[1] A. Saxena, J. Driemeyer, and A. Y. Ng, "Robotic grasping of novel objects using vision," Int. J. Robot. Res, vol. 27, no. 2, pp. 157–173, 2008.

[2] F. Ficuciello et al., "Vision-based grasp learning of an anthropomorphic hand-arm system in a synergy-based control framework," Sci. Robot., vol. 4, no. 26, 2019.

[3] B. T. Nghiem et al., "Providing a sense of touch to prosthetic hands," Plastics and reconstructive surgery, vol. 135, no. 6, pp. 1652-1663, 2015.

[4] M. A. Salas et al., "Proprioceptive and cutaneous sensations in humans elicited by intracortical microstimulation," Elife, vol.7, 2018.

[5] L. Stankov, T. Seizova-Cajić, and R. D. Roberts, "Tactile and kinesthetic perceptual process within the taxonomy of human cognitive abilities," Intelligence, vol. 29, no. 1, pp. 1-29, 2001.

[6] P. M. Wensing et al., "Proprioceptive actuator design in the MIT Cheetah: Impact mitigation and high-bandwidth physical interaction for dynamic legged robots," IEEE Trans. Robot., vol. 33, no. 3, pp. 509-522, 2017.

[7] S. Seok et al., "Design principles for highly efficient quadrupeds and implementation on the MIT Cheetah robot," in Proc. IEEE Int. Conf. Robot. Autom., Karlsruhe, Germany, 2013, pp. 3307-3312.

[8] F. Grimminger et al., "An open torque-controlled modular robot architecture for legged locomotion research," IEEE Robot. Autom. Lett., vol. 5, no. 2, pp. 3650-3657, 2020.

[9] Y. H. Lee et al., "Development of a quadruped robot system with torque-controllable modular actuator unit," IEEE Trans. Ind. Electron., vol. 68, no. 8, pp. 7263-7273, 2020.

[10] M. Hutter et al., "Anymal-a highly mobile and dynamic quadrupedal robot," in Proc. IEEE/RSJ Int. Conf. Intell. Robot. Syst., Daejeon, Korea, 2016, pp. 38-44.

[11] H. Zhu et al., "Design and validation of a partial-assist knee orthosis with compact, backdrivable actuation," in Proc. IEEE 16th Int. Conf. Rehabil. Robot., Toronto, Canada, 2019, pp. 917-924.

[12] U. Kim et al., "Integrated linkage-driven dexterous anthropomorphic robotic hand," Nature Commun., vol. 12, no. 1, 2021.

[13] X. Wu et al., "A Back-Drivable Rotational Force Actuator for Adaptive Grasping," Actuators, vol. 12, no. 7, 2023.

[14] H. Liu et al., "Multisensory five-finger dexterous hand: The DLR/HIT Hand II," in Proc. IEEE/RSJ Int. Conf. Intell. Robot. Syst., Nice, France, 2008, pp. 3692-3697.

[15] D. H. Lee et al., "KITECH-hand: A highly dexterous and modularized robotic hand," IEEE/ASME Trans. Mechatronics, vol. 22, no. 2, pp. 876-887, 2016.

[16] ROBOTIS: AX-12A [Online]. Available: https://www.robotis.com, Accessed: Nov. 24, 2024.

[17] HIGHEST: B500H-Mini [Online]. Available: https://highestrc.com, Accessed: Nov. 24, 2024.

[18] ROBOTIS: XL-320 [Online]. Available: https://www.robotis.com, Accessed: Nov. 24, 2024.

[19] ROBOTIS: XC-330 [Online]. Available: https://www.robotis.com, Accessed: Nov. 24, 2024.

[20] P. L. Garcia et al., "Factors influencing actuator's backdrivability in human-centered robotics," MATEC Web of Conferences, vol. 366, 2022.

[21] J. E. Besong and Y. Fujimoto, "Design of a Coreless Multi-Phase Electric Motor Using Magnetic Resonant Coupling," IEEE Trans. Magn., vol. 58, no. 9, pp. 1-11, 2022.

[22] D. Kim et al., "Neural Network-Based Joint Velocity Estimation Method for Improving Robot Control Performance," IEEE Access, vol. 11, pp. 130517-130526, 2023.

[23] S. M. Yang and S. J. Ke, "Performance evaluation of a velocity observer for accurate velocity estimation of servo motor drives," IEEE Trans. Ind. Appl., vol. 36, no. 1, pp. 98–104, 2000.

[24] C. Elisei-Iliescu et al., "A recursive least-squares algorithm for the identification of trilinear forms," Algorithms, vol. 13, no. 6, p. 135, 2020.

[25] A. Tsuchiya and T. Murakami, "Characteristic analysis of feedback control system with simplified disturbance compensator," in Proc. IECON'03 - 29th Annual Conf. IEEE Ind. Electron. Soc., vol. 3, IEEE, 2003, pp. 2817-2822.

[26] E. Sariyildiz and K. Ohnishi, "An adaptive reaction force observer design," IEEE/ASME Trans. Mechatronics, vol. 20, no. 2, pp. 750-760, 2014.

[27] H. Zhao et al., "Optoelectronically innervated soft prosthetic hand via stretchable optical waveguides," Sci. Robot., vol. 1, no. 1, 2016.